Author/s:
Hay, MA;Gable, RW;Boskovic, C

Title:
Modulating the electronic properties of divalent lanthanoid complexes with subtle ligand tuning

Date:
2023-02-14

Citation:
Hay, M. A., Gable, R. W. & Boskovic, C. (2023). Modulating the electronic properties of divalent lanthanoid complexes with subtle ligand tuning. Dalton Transactions, 52 (11), pp.3315-3324. https://doi.org/10.1039/d2dt03782c.

Persistent Link:
https://hdl.handle.net/11343/333021

Modulating the electronic properties of divalent lanthanoid complexes with subtle ligand tuning†

*Moya A. Hay, Robert W. Gable, Colette Boskovic**

School of Chemistry, University of Melbourne, Parkville, Victoria 3010, Australia

E-mail: c.boskovic@unimelb.edu.au

Abstract

Five new compounds of formula $[Ln^{II}(Me_ntpa)_2](BPh_4)_2$ (Ln = Eu, n = 0 (**1-Eu**), n = 2 (**2-Eu**) and n = 3 (**3-Eu**); Ln = Yb, n = 0 (**1-Yb**) and n = 2 (**2-Yb**); tpa = tris(2-pyridylmethyl)amine, n = 0–3 corresponds to successive methylation of the 6-position of the pyridine rings of Me_ntpa) have been synthesized and their structural, photophysical and electrochemical properties investigated. The Ln^{II} ions in the five complexes possess cubic coordination geometry and exhibit only small structural differences, due to the lengthening of the Ln-N bonds to accommodate the additional steric bulk associated with increasing methylation of the Me_ntpa ligands. Photophysical studies indicate moderate shifts in absorbance, emission and excitation bands associated with the $4f^7 \leftrightarrow 4f^65d^1$ (Eu^{II}) and $4f^{14} \leftrightarrow 4f^{13}5d^1$ (Yb^{II}) transitions, while electrochemistry reveals modulation of the redox potential of the Ln^{II} to Ln^{III} oxidation. There is a strong correlation between Ln-N bond lengths and both the photophysical transition energies and metal redox-potentials, revealing how subtle ligand changes and ligand field effects can be used to modulate the electronic properties of complexes of divalent lanthanoid ions. Utilization of these insights may ultimately afford design and property modulation strategies for future functional molecular complexes based on divalent lanthanoid metals.

Introduction

Advances in lanthanoid-based molecular materials rely on a fundamental understanding of the electronic structure and resulting photophysical, magnetic and redox properties.[1–7] Although lanthanoid (Ln) ions have mainly been considered in the trivalent form in which they are most stable, the divalent oxidation state presents an enticing area for exploration and is receiving increased attention in different avenues of research.[4,6,8–14] For Ln^{II}, our understanding of properties at the molecular level is mostly based on Eu^{II}, the most accessible divalent ion. The Eu^{II} ion has been investigated primarily due to its interesting luminescence behavior and large magnetic moment, with recent reports of luminescence thermometry, imaging contrast agents and photoredox catalysis.[15–18] Ytterbium and samarium, which are the next most accessible in the divalent oxidation state, have also been investigated with particularly focus on reactivity and small-molecule activation.[18–20] Despite the challenges with redox accessibility for the rest of the series, molecular species have been isolated for all of the divalent lanthanoid ions except Pm.[21,22]

The electronic structure of the divalent lanthanoid ions differs from that of their trivalent counterparts, in the relatively low energy of the 5d orbitals. The energy lowering of the 5d orbitals of the free divalent versus the trivalent ion is due to the higher coulombic repulsion associated with adding an extra electron into the 4f orbitals of the ground state. Consequently, Ln^{II} ions may adopt a $4f^{n+1}$ or $4f^n5d^1$ configuration.[3,21–23] For Eu^{II} and Yb^{II}, a preference for $4f^7$ (Eu) and $4f^{14}$ (Yb) configurations is driven by the stability of forming a half-full and full *f*-shell, respectively. Consequently, the $4f^{n+1} \leftrightarrow 4f^n5d^1$ transition is usually located in the UV-visible range, and often these compounds will have distinctively intense colors, in contrast to their trivalent equivalents.[24–26] If non-radiative relaxation can be controlled, emission from the $4f^n5d^1$ excited state can also be observed in the visible region without the need for a sensitizing antenna ligand,[12] as is required for

the trivalent compounds, making them particularly attractive for photophysical based applications. The 5d orbitals interact with the surrounding ligand field and strong ligand field splitting can lead to significant energy lowering of the lowest lying 5d orbitals.[23,27] This interaction is much greater than for 4f orbitals and thus the Ln^{II} electronic structure, and therefore emission and related properties, can be tuned by ligand variation, in a manner more commonly associated with d-block metals.[27–29] The opportunity to tune the properties at a molecular level using the surrounding ligand field is a major incentive for the investigation of complexes of divalent lanthanoid ions.

Despite the promise of their physical and chemical properties, investigation of Ln^{II} ions has been much more prevalent in the solid state than in solution due to poor oxidative stability, and thus understanding of isolated molecular species of Ln^{II} in solution remains limited. Most studies have involved Eu^{II} encapsulated with macrocyclic ligands, such as crown-ether or cryptand ligands, to enhance oxidative stability.[26–30] As the divalent lanthanoid ions can exhibit luminescence, encapsulating the Ln^{II} ion can also help minimize the solvent interactions that can lead to non-radiative relaxation. Reports of this behavior in the solution state are limited, with the exception of Eu^{II} cryptates, and enhancing understanding of how to control the electronic and redox properties of Ln^{II} ions requires further systematic studies. Studies carried out to date have tended to involve substantial changes to the ligand scaffolds (*e.g.* changing donor atoms),[27,31] which raises the question as to whether it possible to tune the electronic properties in a more controlled way with more subtle forms of ligand tuning. A relevant series of elegant studies comes from the work of Anderson, Morris and coworkers, who showed that derivitization of redox-active 2,2'-bipyridyl ligands can control the electronic structure of heteroleptic ytterbocene bipyridine complexes.[4,32–35]

In this work we sought to employ the tris(2-pyridylmethyl)amine (tpa) ligand family, with tpa previously shown to coordinate to Ln^{III} in both homo- and heteroleptic compounds.[36–40] Specifically relevant to the present work, tpa has also been reported previously by Mazzanti *et al.* to coordinate Eu^{II} and Yb^{II} in the compounds $[Ln^{II}(tpa)_2][I_2]$.[39] In the present study we sought to explore Me_ntpa (n = 0-3) ligands derived from sequential methylation of the 6-position of the pyridine rings of the tpa ligand. The ability of these ligands to tune the redox potential of d-block metals is well known,[41–45] and we were interested to see if this could be applied to f-block Ln^{II} complexes. Some of us and others have made use of the ability of the more highly methylated Me_ntpa (n = 2 and 3) ligands to stabilize lower valent metal ion redox partners such as Cu^{I}, Fe^{II} and Co^{II} versus the stabilization of higher valent Cu^{II}, Fe^{III} and Co^{III} by less methylated Me_ntpa (n = 0 and 1).[41,42,45–49] This effect is largely controlled by the steric requirements of the ligand, with accommodation of the additional methyl groups requiring the longer metal-donor atom bond lengths associated with the lower valent metals and affording a weaker ligand field. This electronic tuning strategy has been very beneficial in targeting switchable functional behaviors such as valence tautomerism (an intramolecular charge transfer between redox-active metal and ligand) in cobalt-dioxolene systems, which are of interest for future materials applications.[50,51] It might be anticipated then that if the redox-tuning ability of these ligands were translated to the lanthanoid ions, it could allow access to controlled switchable behavior and lead to the development of novel lanthanoid-based molecular materials.

To explore this possibility further, we elected to elaborate on the handful of known lanthanoid complexes of tpa ligands and investigate a series of compounds with general formula $[Ln^{II}(Me_ntpa)_2](BPh_4)_2$ (Ln = Eu, Yb; n = 0, 2 and 3). The $[Ln^{II}(tpa)_2](BPh_4)_2$ compound reported herein is related to the previously described $[Ln^{II}(tpa)_2]I_2$,[39] but with a different counterion

modifying the overall crystal lattice. By subtly changing the ligand framework with controlled introduction of methyl groups, while maintaining a consistent geometry across the series, we sought to understand the effect on the electronic (spectroscopic and redox) properties of this family of compounds.

Experimental

Materials and methods

All synthetic methods and solution studies were performed under anaerobic conditions (N_2 atmosphere) using standard Schlenk and glove box techniques, unless otherwise indicated. All chemicals purchased were of reagent grade or higher and used as received, except tetrahydrofuran (THF) and diethyl ether which were dried and degassed using an MBraun SPS 7 system. Other solvents were dried over molecular sieves (3 Å) for 3 days and stored under N_2 until used. Solvents were degassed prior to use via the freeze-pump-thaw method. All ligands (Me_ntpa where n = 0, 2 and 3) were synthesized per previously reported procedures,[42,45] with modifications to the synthesis of Me_3tpa enabling us to conduct the hydrogenation with aid of a Schlenk line and under ambient pressures.

Synthesis

$[Eu(tpa)_2](BPh_4)_2$ (1-Eu) With the use of Schlenk-line, an equimolar (0.20 mmol) acetonitrile (MeCN) solution (5 ml) of tpa and $NaBPh_4$ was slowly added to a suspension of LnI_2 (0.10 mmol) in MeCN (5 ml). The resulting deep red solution was then stirred at room temperature for a further 15 minutes before reducing to half volume and placing in the freezer. Dark red crystals suitable for single crystal X-ray diffraction were formed after 3 days and analyzed as $[Eu(tpa)_2](BPh_4)_2$. To obtain a bulk crystalline sample, two vials were prepared in the glovebox – one containing equimolar amounts (0.20 mmol) of tpa and $NaBPh_4$ in MeCN (5 ml), and the other containing a stoichiometric amount of LnI_2 (0.10 mmol) suspended in THF (5 ml). The MeCN solution was the carefully layered on top of the Eu-containing THF solution. The vial was then sealed using electrical tape to prevent loss of solvent. After one week, the dark red crystalline material was

collected from the vial and washed with MeCN to ensure any undissolved reagents were removed and dried under a purge cycle in the glovebox. The bulk sample analyzed as $[Eu^{II}(tpa)_2](BPh_4)_2$ Yield 77 mg, 55 %. EA: $EuC_{84}H_{76}N_8B_2$ [%], found: C 73.38, H 5.63, N 8.01; calc: C 73.58, H 5.59, N 8.17. Selected FT-IR data (ν in cm^{-1}): 1599 (s), 1576 (m), 1478 (s), 1435 (s), 1372 (m), 1258 (m), 1153 (m), 1004 (s), 839 (m), 764 (vs), 733 (vs), 703 (vs), 611 (s).

$[Eu(Me_2tpa)_2](BPh_4)_2$ (2-Eu) The synthetic method followed that of **1-Eu** with bright orange plate crystals isolated from a bright orange solution, with structural analysis indicating the formula $[Eu^{II}(Me_2tpa)_2](BPh_4)_2$, while the bulk crystalline sample is slightly hygroscopic, analyzing as **2-Eu**·H_2O. Yield 52 mg, 36 %. EA: $EuC_{88}H_{84}N_8B_2 \cdot H_2O$ [%], found: C 73.22, H 5.94, N 7.67; calc: C 73.23, H 5.87, N 7.76. Selected FT-IR data (ν in cm^{-1}): 1598 (s), 1577 (m), 1460 (m), 1440 (m), 1376 (w), 1094 (m), 999 (w), 839 (w), 794 (m), 735 (vs), 701 (vs), 611 (s).

$[Eu(Me_3tpa)_2](BPh_4)_2$ (3-Eu) The synthetic method followed that of **1-Eu** with bright yellow block crystals isolated from a bright yellow solution, with structural analysis indicating the formula $[Eu^{II}(Me_3tpa)_2](BPh_4)_2$, while the bulk crystalline sample is slightly hygroscopic, analyzing as **3-Eu**·$2H_2O$. Yield 94 mg, 63 %. EA: $EuC_{90}H_{88}N_8B_2 \cdot 2H_2O$ [%], found: C 72.08, H 6.08, N 7.72; calc: C 71.68, H 5.88, N 7.43. Selected FT-IR data (ν in cm^{-1}): 1600 (m), 1575 (m), 1455 (m), 1426 (w), 1374 (w), m, 1164 (m), 1094 (m), 999 (m), 798 (m), 733 (vs), 701 (vs), 609 (s).

$[Yb(tpa)_2](BPh_4)_2$ (1-Yb) The synthetic method followed that of **1-Eu**, without the need to reduce the volume of solution before placing in the freezer. Deep blue-green thick plate crystals were isolated from a deep blue-green solution, with structural analysis indicating the formula $[Yb^{II}(tpa)_2](BPh_4)_2$, while the bulk crystalline sample is slightly hygroscopic, analyzing as **1-Yb** ·$1.5H_2O$. Yield 123 g, 88 %. EA: $YbC_{84}H_{76}N_8B_2 \cdot 1.5H_2O$ [%], found: C 70.69, H 5.42, N 8.04;

calc: C 71.09, H 5.61, N 7.90. Selected FT-IR data (ν in cm^{-1}): 1599 (s), 1576 (m), 1478 (s), 1435 (s), 1372 (m), 1258 (m), 1153 (m), 1004 (s), 839 (m), 764 (vs), 733 (vs), 703 (vs), 611 (s).

$[Yb(Me_2tpa)_2](BPh_4)_2$ (2-Yb) The synthetic method followed that of **1-Yb**, but with excess Me_2tpa (*1 Ln: 2.25Me_2tpa*). Deep purple plate crystals were isolated from a deep purple solution, with structural analysis indicating the formula $[Yb^{II}(Me_2tpa)_2](BPh_4)_2$, while the bulk crystalline sample is slightly hygroscopic, analyzing as **2-Yb**·$1.5H_2O$. Yield 64 mg, 43 %. EA: $YbC_{88}H_{84}N_8B_2$·$1.5H_2O$ [%], found: C 71.39, H 5.84, N 7.77; calc: C 71.64, H 5.94, N 7.59. Selected FT-IR data (ν in cm^{-1}): 1598 (s), 1577 (m), 1460 (m), 1440 (m), 1376 (w), 1094 (m), 999 (w), 839 (w), 794 (m), 735 (vs), 701 (vs), 611 (s).

Crystallography

Single-crystal X-ray diffraction data for **1-Yb**, **2-Eu** and **2-Yb** were collected using a Rigaku Synergy X-ray Diffractometer System using CuKα (λ = 1.5418 Å). The data were reduced using CrysAlisPro software (Version 40.14a), employing a numerical absorption correction based on Gaussian integration over a multifaceted crystal.[52,53] Single-crystal X-ray diffraction data for **1-Eu** and **3-Eu** were collected on the MX1 or MX2 beamline at the Australian Synchrotron,[54,55] tuned to approximately MoKα radiation (λ = 0.71073 Å) fitted with a silicon double crystal monochromator. Data reduction was performed using XDS, using strong multi-scan absorption correction in SADABS.[56] Crystals were transferred directly from the mother liquor to crystallographic oil to prevent crystallinity/solvent loss. Structures were solved using SHELXT[57] routine and refined using a full matrix least squared procedure based on F^2 using SHELXL within OLEX2.[57–60] Additional refinement details are available in the Supporting Information. Powder X-ray diffraction (PXRD) data were measured on a Rigaku Synergy Dual Wavelength Rotating

Anode X-ray Diffractometer System using CuKα (λ = 1.5418 Å) at room temperature. Powder samples were prepared by grinding the dry bulk samples and loading into a borosilicate glass capillary for measurement. Data were collected between $5 < 2\theta < 50°$ with an exposure time of 120 seconds per frame and processed using CrysAlisPro.

Elemental analysis

The C, H, N analyses were performed at the Campbell Microanalytical Laboratory, University of Otago.

Thermogravimetric analysis

All analyses were performed on a Mettler Toledo TGA/SDTA851e using a ramp rate of 5 °C min^{-1} to a maximum temperature of 400 °C in a flow of N_2 or air (as specified).

Electrochemistry

Cyclic voltammetry was conducted using a standard three-electrode cell configuration under a N_2 atmosphere, using a 1 mm diameter glassy-carbon electrode, a Ti-coated Pt wire auxiliary electrode, and a leak-free Ag/AgCl reference electrode calibrated against the Fc/Fc^+ couple. All measurements were undertaken at an analyte concentration of 0.5 mM in 10 ml MeCN with 0.25 M Bu_4NPF_6 as the supporting electrolyte. Solutions were transferred to the electrochemistry cell by cannula transfer from Schlenk flasks containing the prepared solutions. At all stages we attempted to keep the cell and solution under inert atmosphere, however due to restrictions in our experimental set up, difficulties were encountered in preventing the extremely facile oxidation of **2-Yb**, which is immediately apparent from color change of the solution.

Solution electronic spectroscopy

All samples were prepared in a glove box under an N_2 atmosphere, transferred to quartz cuvettes equipped with screw-top caps, and sealed with electrical tape.[61] All solutions were measured on an Agilent Technology Cary 60 UV-Visible spectrometer. Excitation and emission spectra were recorded using an Agilent Cary Eclipse Fluorescence Spectrophotometer.

Solid state electronic spectroscopy

Diffuse reflectance UV-visible spectra were measured on the samples diluted ~5% in KBr on a Thermo Scientific Evolution 220 UV-visible spectrophotometer. Solid-state attenuated total reflectance infrared spectra were measured on a Bruker Alpha spectrometer and normalized as absorbance spectra.

Results and discussion

Synthesis

Compounds **1-Eu**, **2-Eu**, **3-Eu** and **1-Yb** were all synthesized using the same method, involving the combination of the reagents in stoichiometric amounts (Scheme 1). Analogues using the mono-methylated (Metpa) ligand were not attempted due to synthetic difficulties in purifying this ligand as well as previous studies having shown that the variation across the Me$_n$tpa series can be satisfactorily illustrated without these compounds.[46,47] Compound **2-Yb** however required a slight excess of ligand to deter the formation of heteroleptic compound [$Yb^{II}I_2$(Me$_2$tpa)] (also isolated during the reaction of YbI_2 with Me$_3$tpa), presumably due to the smaller size of Yb versus Eu. The synthesis of **1-Eu** and **1-Yb** differs from the reported synthesis of the iodide salts mainly by the

incorporation of $NaBPh_4$ into the reaction mixture to afford the tetraphenylborate salts.[39] The difference in ionic radii became challenging when pursuing the synthesis of $[Yb(Me_3tpa)_2](BPh_4)_2$ which could not be isolated, despite attempts with varying amounts of excess ligand. Multiple attempts instead yielded crystals of the heteroleptic complexes $[YbI_2(Me_3tpa)]$ and $[Yb(Me_3tpa)(MeCN)_3]^{2+}$, which likely reflects the inability of the relatively smaller Yb^{II} ion to accommodate two sterically bulky Me_3tpa ligands.

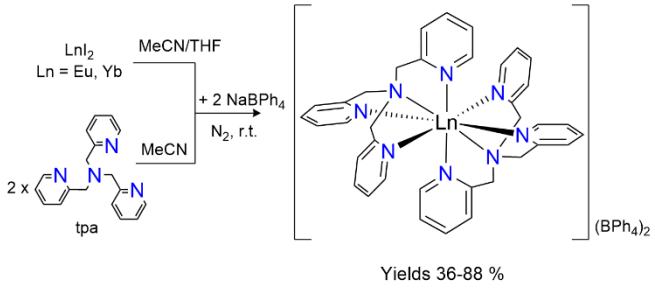

Yields 36-88 %

$[Eu(tpa)_2](BPh_4)_2$	(**1-Eu**)
$[Eu(Me_2tpa)_2](BPh_4)_2$	(**2-Eu**)
$[Eu(Me_3tpa)_2](BPh_4)_2$	(**3-Eu**)
$[Yb(tpa)_2](BPh_4)_2$	(**1-Yb**)
$[Yb(Me_2tpa)_2](BPh_4)_2$	(**2-Yb**)

Scheme 1 General synthetic scheme for compounds reported herein using the unsubstituted tpa ligand as an example (note: **2-Yb** required a slight excess of the ligand Me_2tpa).

Two methods - one for single crystals and one for bulk crystalline samples - were pursued due to the ease of collection of single crystals from Schlenk flasks versus the glovebox, with the freezer significantly improving the crystal quality and time required for crystallization to occur. Despite differences, the comparison of the powder X-ray diffraction pattern of the bulk crystalline product and that simulated from the single-crystal data showed an exceptional match, suggesting

phase purity (Fig. S1 – S3†). In general, the solid crystalline samples of all compounds showed some air-stability, allowing us to prepare the powder X-ray diffraction samples in air without visible oxidation or decomposition. The solid-state infrared spectra (ATR) of compounds **1-Ln**, **2-Ln** and **3-Eu** are very similar (Fig. S4†), consistent with the similar molecular structures of the series. Elemental analyses were also consistent with purity of the bulk samples, although some of the samples showed signs of hygroscopicity, noting that the samples for microanalysis were prepared in ambient air. Thermogravimetric analyses performed under flow of N_2 (Fig. S5†), indicated no solvation of the sample, consistent with the single-crystal X-ray diffraction measurements. Thermogravimetric analyses performed in air (Fig S6†) are consistent with loss of small amounts of water and thus the hygroscopicity observed by elemental analysis.

Crystal Structures

Crystallographic data and refinement parameters are presented in Tables S1† and S2†. As the compounds with analogous ligands are isostructural (**1-Eu** and **1-Yb**; **2-Eu** and **2-Yb**) they are discussed collectively. Compounds **1-Ln** crystallize in the monoclinic $P2_1/n$ space group, in contrast to **2-Ln** and **3-Eu**, which crystallize in the triclinic P-1 space group, with the lowering of symmetry attributed to the presence the bulky methyl groups that introduce crystallographic disorder. In all cases, the divalent Ln center is 8-coordinate (Fig. 1, Fig. S7†, Fig. S8† and Fig S9†). Continuous shape measures using the software SHAPE 2.1 were employed to determine the geometry of the Ln centers[62,63] and suggest that the coordination geometry is closest to cubic in all cases. The Shape distortion parameters (Tables 1 and S3†) are in the range 0.69-1.53 for the cubic geometry, where the further the value is from zero, the greater the distortion from ideal geometry.

The next lowest Shape distortion parameters are in the range 1.63-2.46 for triakis tetrahedral coordination. The cubic coordination geometry is a rare for lanthanoid ions.[64,65] The two tetradentate Me_ntpa ligand moieties complete the Ln^{II} coordination sphere. For both **1-Ln** and **2-Ln**, half a molecule resides in the asymmetric unit along with a tetraphenylborate counterion, as opposed to **3-Eu**, which has crystallographically inequivalent ligands, and a full molecule in the asymmetric unit.

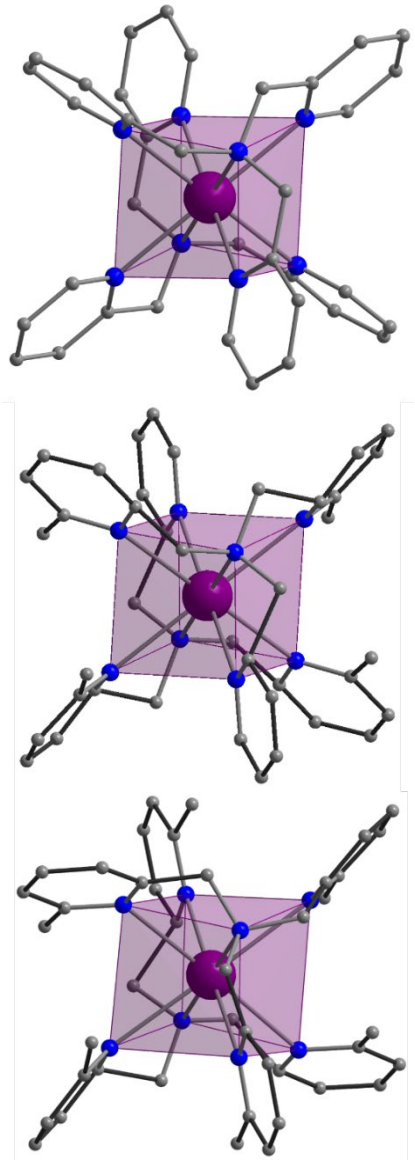

Fig. 1 Molecular structures of Eu complexes in **1-Eu** (top), **2-Eu** (middle) and **3-Eu** (bottom), highlighting approximate cubic coordination. Hydrogen atoms have been omitted for clarity. Color code: Eu (violet), N (blue), C (grey).

Table 1 Selected interatomic distances (Å) and SHAPE distortion parameter (cubic coordination geometry) values for **1-Ln**, **2-Ln** and **3-Ln**.

	1-Eu	**2-Eu**	**3-Eu**	**1-Yb**	**2-Yb**
Ln1-N1'[a]	2.726(2)	2.718(7)	2.702(6)	2.628(4)	2.617(6)
Ln1-N2'	2.697(3)	2.776(6)	2.857(3)	2.602(1)	2.694(6)
Ln1-N3'	2.682(8)	2.741(6)	2.806(5)	2.584(4)	2.665(6)
Ln1-N4'	2.695(3)	2.792(7)	2.851(3)	2.607 (5)	2.758(7)
Ln1-N_{avg}	2.700	2.757	2.804	2.605	2.684
N1···N1'	5.432(3)	5.459(9)	5.433(3)	5.257(3)	5.251(14)
Ln···Ln[b]	12.724(3)	11.055(2)	11.108(5)	12.318(11)	11.048(2)
SHAPE[c]	1.527	1.037	1.087	0.958	0.687

'For **1-Ln** and **1-Eu**: 1-X,1-Y,1-Z; **2-Ln**: X,-Y,1-Z.' [a] N1 is the amine nitrogen of Me$_n$tpa. [b] Closest intermolecular distance. [c] *SHAPE* index for cube geometry (8-coordinate) in *SHAPE 2.1*.

For all compounds, the Me$_n$tpa ligands adopt a staggered conformation around the Ln center to reduce steric clash between the pyridyl arms (Fig. S8†). For **2-Ln** and **3-Eu**, the methyl substituents then occupy the space between the pyridyl arms, effectively encapsulating the Ln^{II} ion. The staggered conformation has consequences in terms of the geometric distortion and Ln-N bond lengths, as well as the steric hindrance around the Ln^{II} center, with relevant parameters presented in Table S1. Distortion away from the ideal coordination geometry can be quantified by the deviation of the SHAPE distortion parameter from zero. The Yb analogues are less distorted than their Eu counterparts, due to the smaller ionic radius of Yb^{II} versus Eu^{II}. This is also reflected in the shorter Ln-N_{avg} bond lengths for the Yb analogues, consistent with the previously reported for $[Ln^{II}(tpa)_2][I_2]$ (Ln = Eu, Yb).[39] The presence of the Me$_n$tpa methyl substituents for **2-Ln** and **3-Eu** results in increasing Ln-N bond lengths in the order: **1-Yb** < **2-Yb** < **1-Eu** < **2-Eu** < **3-Eu**. The increased electronic donation from the methyl groups might be expected to result in an increased ligand field, hence a shortening of the Ln-N bonds, however the opposite trend is observed. Although no such analogous Me$_n$tpa families have been reported previously for the

lanthanoids, similar trends have been observed for various 3d transition metals, including Cu, Fe and Co, where in each case the M-N bond lengths increase in the order tpa < Me_2tpa < Me_3tpa.[41,42,44,45,49] This is attributed to the M-N bonds increasing to accommodate the steric requirements of the additional methyl substituents. Overall, this suggests the electronic effects of the methyl groups are dominated by the steric effects for metal complexes of the Me_ntpa family of ligands. The shorter bond-lengths for **1-Ln** are suggestive of a stronger ligand field, allowing for better metal-ligand orbital overlap, and therefore greater ligand interaction with the 5d orbitals in the $4f^n5d^1$ excited state. The increased Ln-N bond lengths with increased tpa methylation is also accompanied by a decrease in distortion from ideal cubic geometry (Table 1), which could be due to the locking of the ligand conformation by the bulky methyl groups, inhibiting movement of the ligand around the Ln^{II} center.

The consistency in the geometries exhibited by the series of compounds discussed here presents an opportunity to study the effect of subtle changes to the ligand scaffold on the molecular structure, electronic structure and resulting electronic properties. To the best of our knowledge, no other studies on Ln^{II} ions have involved modification of the ligand in such a fine-tuned way as to keep the geometry intact across the series, noting that more substantial deviations (e.g., varying donor atom(s) and larger structural changes to the ligand scaffold) render comparison difficult. To probe these ligand effects in, we investigated the photophysical and electrochemical trends for **1-Ln**, **2-Ln** and **3-Eu** to develop an understanding of how these small structural changes modulate the electronic properties.

Photophysical Measurements

The UV-visible absorption spectra of **1-Ln**, **2-Ln** and **3-Eu** in MeCN (Fig. 2 and Fig S10†) remain unchanged under N_2 over a period of at least 3 hours, indicating solution stability within this timeframe. The MeCN solutions are, respectively, dark orange, light orange and yellow for **1-Eu**, **2-Eu** and **3-Eu**; and blue and red for **1-Yb** and **2-Yb**. Exposure of the solutions to air gives rise to rapid color change to a pale yellow, indicative of oxidation of Ln^{II} to Ln^{III}. Furthermore, the MeCN solution absorption spectra and solid-state diffuse reflectance spectra are in good agreement (Figs. S11 – S16†), including the maxima and full-width half-maxima (FWHM) values obtained from multi-peak gaussian fitting (Figs. S12 – S15† and Table S4†), consistent with the maintenance in solution of the solid-state molecular structures. These spectra can provide experimental insight into the nature of the coordination environments in solution, including ligand-field effects and relative strengths of metal-ligand interactions.

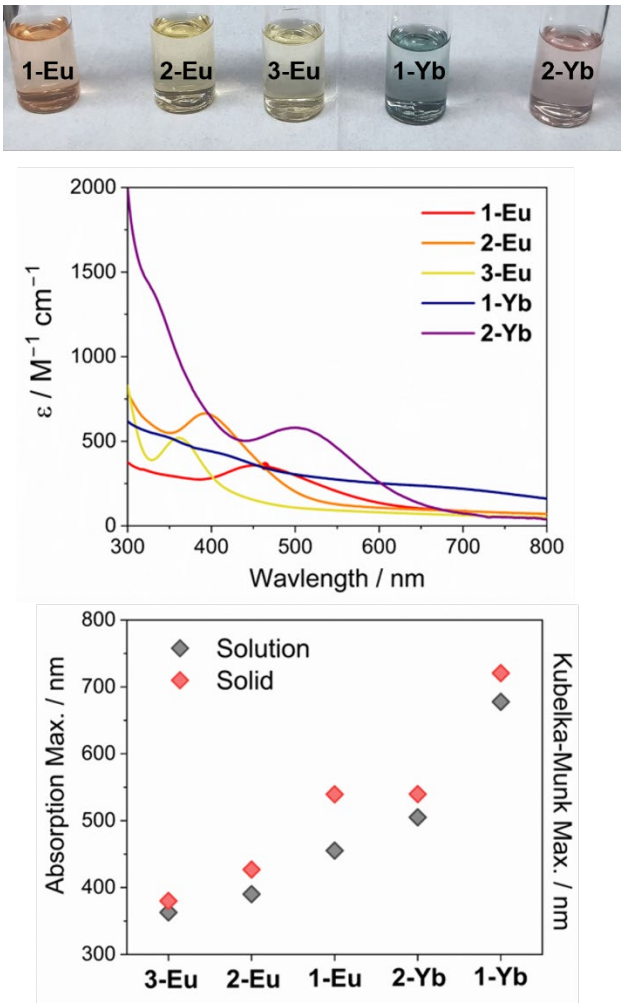

Fig. 2 Solution data for **1-Ln**, **2-Ln** and **3-Ln** in MeCN (0.5 mM): (top) photographs; (middle) UV-visible absorption spectra (color code reflects that of the compounds in both solution and solid state; (bottom) plot of the lowest energy absorption maxima (solution state) together with the lowest energy Kubelka-Munk maxima (solid state).

The absorption spectra of all compounds exhibit broad transitions in the visible range (Table 2) with molar absorptivity expected for Eu^{II} ($^8S_{7/2,}$ $4f^7 \rightarrow 4f^6 5d^1$) and Yb^{II} ($^1S_{0,}$ $4f^{14} \rightarrow 4f^{13}5d^1$).[14,30,66] Inter-ligand transitions are evident in the UV region (250–280 nm), which are also present in the spectra of the free ligands (Fig. S10† and Fig S17†). Another band is also evident in the UV region of each spectrum (~ 200 nm), which is much more intense for the complexes versus the free ligand and suggestive of a metal-ligand charge transfer (MLCT) transition. Bands between 300 and 900 nm occur at different wavelengths depending on the Ln^{II} ion and coordination environment, in accordance with the $4f^n5d^1$ character of the corresponding excited state. The lowest energy absorption maxima (approximately indicative of the energy of the lowest lying 5d orbital) of all complexes are in agreement with values reported previously for amine-rich cryptand ligands and the absorption maxima for the Eu compounds occur at higher energy than for the Yb analogues.[14,22,30,31,67] For both the Eu and Yb series of compounds, the λ_{max} values of the lowest energy absorption maxima decrease in the order: tpa > Me_2tpa > Me_{3t}pa. The trend in λ_{max} for both the Eu and Yb series agrees with the trend in solid state Ln-N bond lengths (Table 2). These trends are consistent with the ligand field splitting of the 5d-orbitals increasing on increasing the ligand field strength from Me_3tpa to tpa,[43] this in turn decreases the gap between the 4f and lowest lying 5d orbitals, hence results in a bathochromic (lower energy) shift of the absorption maxima for stronger field ligands. Thus, the $4f^7 \rightarrow 4f^6 5d^1$ (Eu^{II}) and $4f^{14} \rightarrow 4f^{13}5d^1$ (Yb^{II}) energy gaps are smallest for the tpa analogues **1-Eu** and **1-Yb** and increase on ligand methylation.

Table 2 Structural and solution (MeCN) spectroscopic and electrochemical data for **1-Ln**, **2-Ln** and **3-Ln**: average Ln-N bond lengths (Å); lowest energy absorption maxima (λ_{max}); excitation and emission wavelengths; anodic peak potential E_{pa} (and, if quasi-reversible, half potential $E_{1/2}$) at 100 mVs^{-1} for $Ln^{II} \rightarrow Ln^{III} + e$

Compound	d(Ln-N_{avg}) /Å	λ_{max} /nm (ε /$M^{-1}cm^{-1}$)	λ_{ex} /nm	λ_{em} /nm	E_{pa} ($E_{1/2}$) /V
1-Eu	2.70	455 (357)	383, 398	449, 461	-0.29 (-0.48)
2-Eu	2.76	390 (663)	344	474	-0.10
3-Eu	2.81	363 (518)	327	442	0.08
1-Yb	2.61	678 (238)	303, 328, 355	394, 416, 447	-1.11 (-1.17)
2-Yb	2.68	505 (577)	316, 359	445	-

The 4f-5d transitions important for Ln^{II} are parity allowed and relatively intense and their configurational coordinate diagram indicates relatively broad linewidths and significant Stokes shifts.[12] Shorter bond lengths for the $4f^{n-1}5d^1$ excited states versus the $4f^n$ ground states afford lower emission versus excitation energies (Stokes shifts). The greater interaction of the 5d orbitals with the ligand field affords a wider parabola representing the $4f^{n-1}5d^1$ excited states and broad bands for 4f-5d transitions. The interaction of the 5d orbitals with the ligand field allows 4f-5d transitions to be tuned across the UV, visible and IR ranges. For the present compounds, the encapsulating nature of the bis-Me_ntpa ligand scaffold sterically protects the Ln^{II} center from solvent interactions, even more so with the extra bulk of the methyl groups in the case of Me_2tpa and Me_3tpa. In addition, there are no C-H, N-H, or O-H oscillators in the primary coordination sphere, which should minimize non-radiative relaxation allow for the observation of luminescence.

Therefore, excitation and emission spectra were collected for **1-Ln**, **2-Ln** and **3-Eu** in MeCN (Fig. 3) to further examine the influence of the Me$_n$tpa ligands on the electronic structure of the Ln^{II} ion.

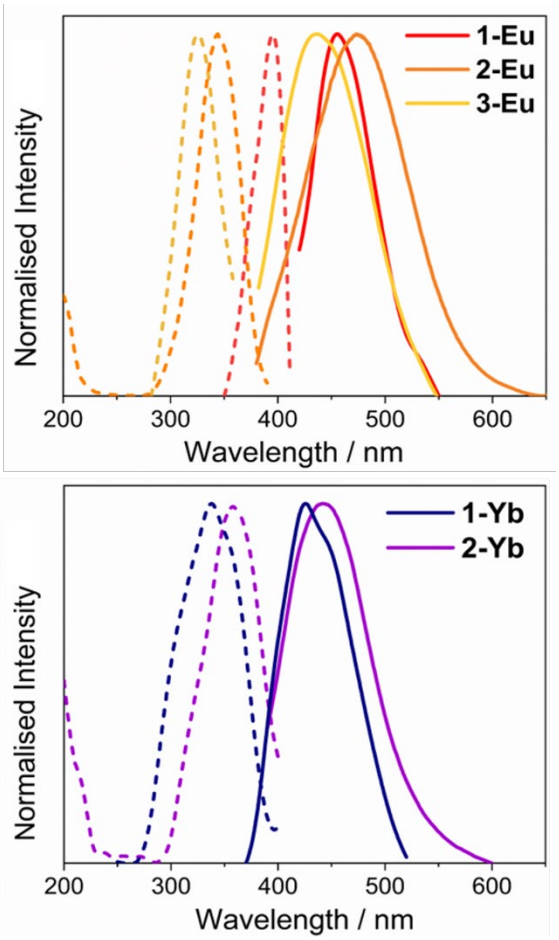

Fig. 3 Excitation (-·-) and emission (—) spectra for MeCN solutions (2 mM) of **1-Eu**, **2-Eu**, and **3-Eu** (top) and **1-Yb** and **2-Yb** (bottom).

All compounds show emission in the visible region, which is again broad in nature due to the spin-orbit interactions inherent to the 4f^{n}5d^1 excited state. The excitation is at higher energies in all cases. As well as an excitation in the visible range characteristic of the 4f^{n+1} $\rightarrow$ 4f^{n}5d^1

transition, a high energy excitation is observed for all compounds (~ 200 nm), at similar energies to the band observed in the absorption spectra and attributed to a MLCT process. Regardless of excitation, the maximum emission wavelength did not change, suggesting that emission only occurs from the $4f^n5d^1$ state, although in some cases the emission and excitation bands appeared to be comprised of multiple overlapping bands. Thus, both excitation and emission bands (> 300 nm) were fit using a multi-peak Gaussian function to extract peak positions and full width at half maximum (FWHM) values associated with the direct $4f^{n+1} \leftrightarrow 4f^n5d^1$ excitation and emission processes (Figs. S18 – S22†; Table S5†). For **2-Eu** and **3-Eu**, both excitation and emission bands could be fit to a single peak, however for **1-Eu**, **1-Yb**, and **2-Yb**, it was necessary to fit the data to multiple maxima. This is consistent with the absorption spectra, which suggests the lowest lying 5d orbitals are at lower energy for **1-Eu**, **1-Yb**, and **2-Yb**. Additionally, for **1-Eu** and **1-Yb**, the different peaks exhibit a greater separation, corresponding to the larger splitting of the d-orbitals because of the stronger ligand field of tpa versus Me_ntpa (n = 2 and 3).

Broad emission is evident in the visible range 380-600 nm for **1-Eu**, **2-Eu** and **3-Eu** with excitation maxima in the range 280–410 nm. The trend in excitation maxima of the Eu^{II} series follows that of the lowest energy absorption maxima, with **3-Eu** exciting at the highest energy. However, the trend is not emulated in the emission maxima. In contrast, the trend in excitation maxima for the Yb^{II} series is opposite that of the absorption maxima trend, while the trend in emission maxima follows that of the excitation maxima. The relative similarity in emission maxima for analogous Eu and Yb complexes is consistent with literature observations for Eu^{II} and Yb^{II} cryptand complexes.[14] Although **2-Eu** and **3-Eu** show a similar Stokes shift (130 nm for **2-Eu** and 115 for **3-Eu**), **1-Eu** with the bare tpa ligand scaffold shows a smaller average Stokes shift of 64 nm. This contrasts with the Yb analogues, which both exhibit similar Stokes shifts (92 nm

1-Yb vs 86 nm for **2-Yb**). The larger Stokes shifts for **2-Eu** and **3-Eu** suggest that these compounds possess the largest difference in bond lengths between the ground and excited states, noting that **2-Eu** and **3-Eu** already exhibit the longest Ln-N bond lengths in the ground state for this family of complexes.

The observed variations in the maximum wavelengths of the bands across each series and between the two series are difficult to rationalize as the emissive properties of Ln^{II} complexes are not so well understood and relatively few examples of comparative photophysical studies of analogous Eu^{II} and Yb^{II} coordination complexes are available in the literature.[14,68] The Stokes shift is larger for a literature Yb^{II} tris(silylamide) complex than for the Eu^{II} analogue,[68] which is not consistent with the present study. The trends in emission maxima for a family of Ln^{II} cryptand complexes differ for the Yb^{II} complexes in comparison to the Eu^{II} analogues, as also occurs for **1-Ln** and **2-Ln**, while as in the present case, the trends in absorption maxima are the same for the Eu^{II} and Yb^{II} analogues. While clear trends are observed and can be readily explained for the absorption maxima, the origin of the lack of equivalent trends for the emission and excitation maxima remains unknown. Particularly puzzling is that the emission peaks of **1-Yb** and **2-Yb** are far more blue-shifted compared to the absorption maxima. Given that the d-f transition for Yb^{II} is spin-forbidden, it might be that the emission of **1-Yb** and **2-Yb** instead originates from MLCT or inter-ligand transitions.

Electrochemistry

Following confirmation of solution stability via electronic absorption spectroscopy, cyclic voltammograms were measured for MeCN solutions of **1-Ln**, **2-Eu**, and **3-Eu** (0.5 mM of analyte;

0.25 M $TBAPF_6$) using a glassy carbon electrode (Fig. 4 and Figs. S23-25†). All potentials are referenced to the ferrocene/ferrocenium couple (Fc/Fc^+). In each case the initial potential was selected to coincide with the open circuit potential. It was not possible to obtain a measurement for **2-Yb**, due to rapid oxidation in solution in the electrochemical cell, despite efforts taken to exclude oxygen.

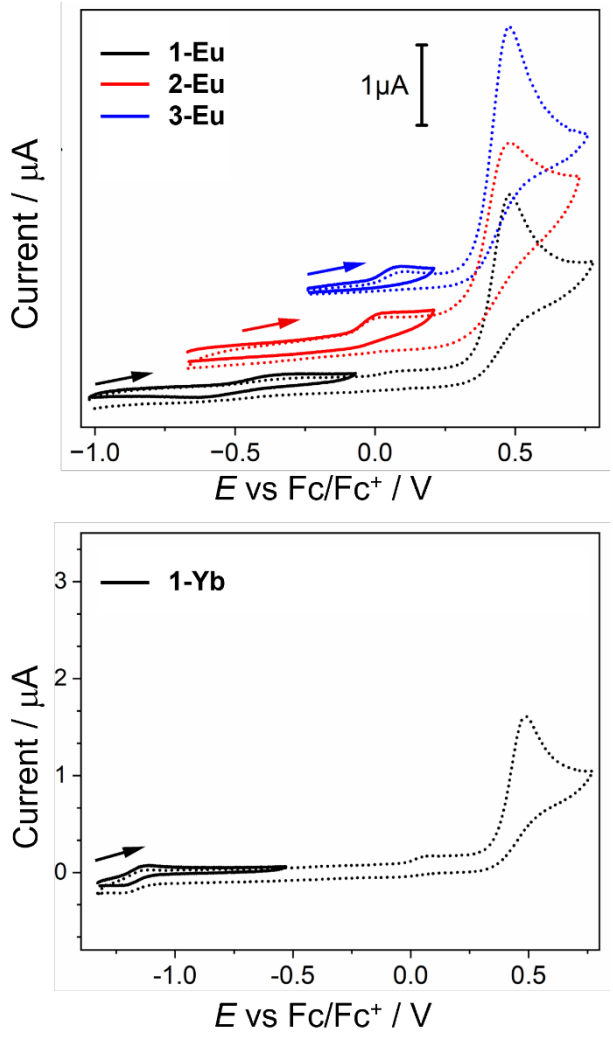

Fig. 4 Cyclic voltammograms of **1-Eu**, **2-Eu**, **3-Eu** and **1-Yb** (0.5 mM in MeCN with 0.25 M Bu_4NPF_6; scan rate of 100 mVs^{-1}). The dotted lines represent the full scan through all observed

processes; the solid lines are the voltammograms obtained with switching prior to the second oxidation. Arrows indicate the direction of the scan.

Cyclic voltammograms measured for **1-Yb, 1-Eu**, **2-Eu** and **3-Eu** (Fig. 4 and Figs. S22-24†) reveal in each case two oxidation processes within the accessible potential window. An irreversible process with an anodic peak potential (E_{pa}) of 0.48 V at a scan rate of 100 mVs^{-1} is consistently observed across all measured compounds and corresponds to the oxidation of the tetraphenylborate counterion present in solution.[69] The four compounds each exhibit an additional lower potential oxidation process at varying potentials, which is assigned as the one-electron oxidation of Ln^{II} to Ln^{III} (Table 2). For tpa compounds **1-Eu** and **1-Yb** (Fig. S26†), the low potential process is quasi-reversible with respective half-potentials ($E_{1/2}$) of –0.48 and –1.17 V and peak to peak separations (ΔE_p) at 100 mVs^{-1} of 280 and 90 mV. The quasi-reversibility indicates some stability of the oxidized analogues $[Ln^{III}(tpa)_2]^{3+}$ for both Eu and Yb. The $E_{1/2}$ values are in excellent agreement with the values of –0.41 and –1.17 V previously reported for the corresponding one-electron Ln^{III} to Ln^{II} reduction processes in $[Eu(tpa)_2]OTf_3$ and $[Yb(tpa)_2]OTf_3$ (OTf^- = triflate), prepared in situ, but not isolated.[39] The Eu-centered process for **2-Eu** and **3-Eu** is electrochemically irreversible, and occurs at more positive potentials compared to **1-Eu**, with anodic peak potentials (E_{pa}) at 100 mVs^{-1} scan rate of – 0.10 V for **2-Eu** and 0.08 V for **3-Eu** versus -0.29 V for **1-Eu**. The irreversibility of these oxidations for **2-Eu** and **3-Eu** point to a lack of stability of the oxidized analogues, which may well involve decomplexation of one of the more bulky Me_2tpa or Me_3tpa ligands. We speculate that the inability to prevent oxidation of solutions of **2-Yb** for sufficiently long to measure the voltammetry might be due to oxidation-catalysed decomplexation in the less air-tight electrochemical cell versus the sealed cuvette used to measure

the electronic spectra. This is consistent with the synthetic difficulties experienced in making **2-Yb** and the inability to make the Me_3tpa analogue at all.

The oxidation potential for the one-electron Ln^{II} to Ln^{III} oxidation process increases in the order: **1-Yb** < **1-Eu** < **2-Eu** < **3-Eu**. This is consistent with the much more facile oxidation and relative instability of Yb^{II} compared to Eu^{II}. For the Eu compounds, the trend is indicative of increased stability of Eu^{II} versus Eu^{III} with the degree of methylation of the Me_ntpa ligand. The quasi-reversibility of this oxidation for **1-Yb** and **1-Eu** versus the electrochemical irreversibility for **2-Eu** and **3-Eu** is also consistent with greater stability of the oxidized homoleptic analogues "$[Ln^{III}(Me_n tpa)_2]^{3+}$" for less sterically demanding tpa versus the more highly methylated ligands, give the shorter Ln-N bond lengths for trivalent Ln^{III} versus Ln^{II}. The general trend in redox potentials with degree of methylation of Me_ntpa is entirely consistent with the behavior reported for Me_ntpa complexes of the 3d metals Cu, Fe and Co. [41,42,45–49]

Concluding Remarks

In this work three new homoleptic divalent Eu^{II} and Yb^{II} complexes $[Ln(Me_n tpa)]^{2+}$ (n = 2 and 3) were synthesized and their structural, photophysical and electrochemical properties compared with those of two previously reported $[Ln(tpa)]^{2+}$ analogues to investigate the influence of subtle ligand variation. Structural studies reveal the maintenance of the same molecular structure and cubic coordination geometry across all members of the family. Small variations are evident, associated with differential metal ion size and the lengthening of the bonds between the metal and ligand nitrogen donor atom to accommodate the additional steric bulk on increasing methylation of the Me_ntpa ligands. Indeed, the smaller Yb^{II} ion is unable to accommodate two sterically demanding

Me_3tpa ligands and $[Ln(Me_3tpa)]^{2+}$ could not be synthesized. Photophysical studies for the analogues with different ligands indicate moderate shifts in absorbance, emission and excitation bands associated with the $4f^{n+1} \leftrightarrow 4f^n5d^1$ transitions, while electrochemistry reveals clear modulation of the redox potential of the metal ion. In all cases the behavior can be thought of as steric control of electronic properties, in that the steric requirements of the ligands influence the length of the bonds between the metal and ligand nitrogen atoms, which in turn controls the electronic properties of the metal ion. The metal to nitrogen bond lengths mediate the ligand field experienced by the metal ion and modulate its redox-potential. In the case of the present divalent Eu^{II} and Yb^{II} complexes, the key role played by the $4f^{n-1}5d^1$ first excited state in the photophysical properties allows the variation of the ligand field to influence the observed behavior via the greater susceptibility of the 5d orbitals versus 4f orbitals to ligand field effects.

The key insight from this work is that ligand derivatization strategies to control or modulate the properties of metal complexes that are typically associated with d-block chemistry can be successfully translated to the divalent Ln^{II} ions with energetically accessible $4f^n5d^1$ configurations. Utilization of these insights may afford design pathways and property modulation mechanisms for functional molecular complexes based on divalent Ln^{II} metals. In future work we will explore the possibility of tuning the electronic structure and resulting properties in related heteroleptic complexes, including more detailed characterization of the photoluminescence properties such as quantum yield and lifetime measurements.

Conflicts of Interest

There are no conflicts to declare

Acknowledgments

We would like to thank the Australian Research Council for financial support (DP190100854). This research was undertaken, in part, using the MX1 and MX2 beamlines at the Australian Synchrotron, part of ANSTO, Australia, and made use of the Australian Cancer Research Foundation (ACRF) detector on MX2. We would like to thank Dr Pria Ramkissoon for many helpful discussions regarding lanthanoid luminescence.

† **Electronic Supporting Information (ESI) available**: Details of experimental and synthetic methods, IR, TGA, crystallography, structural analysis, magnetic measurements, UV-vis spectroscopy, excitation and emission spectroscopy, and electrochemistry. CCDC 2178624 – 2178628. For ESI and crystallographic data in CIF or other electronic format see DOI:

References

1 J. C. Wedal and W. J. Evans, *J. Am. Chem. Soc.*, 2021, **143**, 18354–18367.

2 C. A. Gould, K. R. Mcclain, D. Reta, J. G. C. Kragskow, D. A. Marchiori, E. Lachman, E. Choi, J. G. Analytis, R. D. Britt, N. F. Chilton, B. G. Harvey, J. R. Long, U. S. Navy, N. Air, N. Sciences, O. Rd, M. S. Division, L. Berkeley, N. High and M. Field, *Science*, 2021, **202**, 198–202.

3 G. Meyer, *J. Solid State Chem.*, 2019, **270**, 324–334.

4 M. Tricoire, N. Mahieu, T. Simler and G. Nocton, *Chem. – A Eur. J.*, 2021, **17**, 6860–6879.

5 R. L. Halbach, G. Nocton, J. I. Amaro-Estrada, L. Maron, C. H. Booth and R. A. Andersen, *Inorg. Chem.*, 2019, **58**, 12083–12098.

6 M. A. Hay and C. Boskovic, *Chem. - A Eur. J.*, 2021, 1–31.

7 E. Rousset, M. Piccardo, R. W. Gable, M. Massi, L. Sorace, A. Soncini and C. Boskovic, *Inorg. Chem.*, 2022, **61**, 14004–14018.

8 I. V. Lapshin, A. V. Cherkasov, A. F. Asachenko and A. A. Trifonov, *Chem. Commun.*, 2020, **56**, 12913–12916.

9 J. Li, L. Wang, Z. Zhao, B. Sun, G. Zhan, H. Liu, Z. Bian and Z. Liu, *Nat. Commun.*, 2020, **11**, 1–8.

10 H. Qi, Z. Zhao, G. Zhan, B. Sun, W. Yan, C. Wang, L. Wang, Z. Liu, Z. Bian and C. Huang, *Inorg. Chem. Front.*, 2020, **7**, 4593–4599.

11 T. P. Gompa, S. M. Greer, N. T. Rice, N. Jiang, J. Telser, A. Ozarowski, B. W. Stein and H. S. La Pierre, *Inorg. Chem.*, 2021, **60**, 9064–9073.

12 T. C. Jenks and M. J. Allen, in *Modern Applications of Lanthanide Luminescence*, ed. A. de Bettencourt-Dias, Springer, 2021, pp. 67–92.

13 A. R. Willauer, A. M. Dabrowska, R. Scopelliti and M. Mazzanti, *Chem. Commun.*, 2020, **56**, 8936–8939.

14 T. C. Jenks, A. N. W. Kuda-Wedagedara, M. D. Bailey, C. L. Ward and M. J. Allen, *Inorg. Chem.*, 2020, **59**, 2613–2620.

15 R. M. Diaz-Rodriguez, D. A. Gálico, D. Chartrand, E. A. Suturina and M. Murugesu, *J. Am. Chem. Soc.*, 2022, **144**, 912–921.

16 M. D. Bailey, G. X. Jin, F. Carniato, M. Botta and M. J. Allen, *Chem. - A Eur. J.*, 2021, **27**,

3114–3118.

17 T. C. Jenks, M. D. Bailey, J. L. Hovey, S. Fernando, G. Basnayake, M. E. Cross, W. Li and M. J. Allen, *Chem. Sci.*, 2018, **9**, 1273–1278.

18 I. L. Fedushkin, D. S. Yambulatov, A. A. Skatova, E. V. Baranov, S. Demeshko, A. S. Bogomyakov, V. I. Ovcharenko and E. M. Zueva, *Inorg. Chem.*, 2017, **56**, 9825–9833.

19 Y. Zheng, C. S. Cao, W. Ma, T. Chen, B. Wu, C. Yu, Z. Huang, J. Yin, H. S. Hu, J. Li, J. Li, W. X. Zhang and Z. Xi, *J. Am. Chem. Soc.*, 2020, **142**, 10705–10714.

20 G. M. Richardson, I. Douair, S. A. Cameron, L. Maron and M. D. Anker, *Chem. - A Eur. J.*, 2021, **27**, 13144–13148.

21 M. R. Macdonald, E. Bates, J. W. Ziller, F. Furche and W. J. Evans, *J Am Chem Soc*, 2013, **135**, 9857–9868.

22 M. E. Fieser, M. R. Macdonald, B. T. Krull, J. E. Bates, J. W. Ziller, F. Furche and W. J. Evans, *J. Am. Chem. Soc.*, 2015, **137**, 369–382.

23 W. J. Evans, *Organometallics*, 2016, **35**, 3088–3100.

24 N. Sabbatini, M. Ciano, S. Dellonte, A. Bonazzi, F. Bolletta and V. Balzani, *J. Phys. Chem.*, 1984, **4**, 1534–1537.

25 N. Higashiyama, K. Takemura, K. Kimura and G. Adachi, *Inorg. Chim. Acta*, 1992, **194**, 201–206.

26 L. A. Ekanger, D. R. Mills, M. M. Ali, L. A. Polin, Y. Shen, E. M. Haacke and M. J. Allen, *Inorg. Chem.*, 2016, **55**, 9981–9988.

27 T. N. Poe, M. J. Beltrán-Leiva, C. Celis-Barros, W. L. Nelson, J. M. Sperling, R. E. Baumbach, H. Ramanantoanina, M. Speldrich and T. E. Albrecht-Schönzart, *Inorg. Chem.*, 2021, **60**, 7815–7826.

28 R. Barraza, Jr., A. G. Sertage, A. B. Kajjam, C. L. Ward, J. C. Lutter, H. B. Schlegel and M. J. Allen, *Inorg. Chem.*, 2022, **61**, 19649–19657.

29 W. Yan, T. Li, Z. Cai, H. Qi, R. Guo, P. Huo, Z. Liu and Z. Bian, *Inorg. Chem. Front.*, 2022, **9**, 4794–4800.

30 T. C. Jenks, M. D. Bailey, B. A. Corbin, A. N. W. Kuda-Wedagedara, P. D. Martin, H. B. Schlegel, F. A. Rabuffetti and M. J. Allen, *Chem. Commun.*, 2018, **54**, 4545–4548.

31 T. N. Poe, A. N. Gaiser and T. E. Albrecht-Schönzart, *Cryst. Growth Des.*, 2022, **22**, 2670–2678.

32 M. D. Walter, D. J. Berg and R. A. Andersen, *Organometallics*, 2006, **25**, 3228–3237.

33 C. H. Booth, D. Kazhdan, E. L. Werkema, M. D. Walter, W. W. Lukens, E. D. Bauer, Y. J. Hu, L. Maron, O. Eisenstein, M. Head-Gordon and R. A. Andersen, *J. Am. Chem. Soc.*, 2010, **132**, 17537–17549.

34 G. Nocton, C. H. Booth, L. Maron and R. A. Andersen, *Organometallics*, 2013, **32**, 5305–5312.

35 R. E. Da Re, C. J. Kuehl, M. G. Brown, R. C. Rocha, E. D. Bauer, K. D. John, D. E. Morris, A. P. Shreve and J. L. Sarrao, *Inorg. Chem.*, 2003, **42**, 5551–5559.

36 R. Wietzke, M. Mazzanti, J. M. Latour, J. Pécaut, P. Y. Cordier and C. Madic, *Inorg. Chem.*, 1998, **37**, 6690–6697.

37 L. Natrajan, J. Pécaut, M. Mazzanti and C. LeBrun, *Inorg. Chem.*, 2005, **44**, 4756–4765.

38 T. Yamada, S. Shinoda and H. Tsukube, *Chem. Commun.*, 2002, **2**, 1218–1219.

39 J. Andrez, G. G. Bozoklu, G. G. G. Nocton, J. Pécaut, R. Scopelliti, L. Dubois, M. Mazzanti, J. Pecaut, R. Scopelliti, L. Dubois, M. Mazzanti, J. Pøcaut and R. Scopelliti, *Chem. - A Eur. J.*, 2015, **21**, 15188–15200.

40 X. Zhang, H. Xie, M. Ballesteros-Rivas, T. J. Woods and K. R. Dunbar, *Chem. - A Eur. J.*, 2017, **23**, 7448–7452.

41 S. E. Cheyne, L. F. McClintock and A. G. Blackman, *Inorg. Chem.*, 2006, **45**, 2610–8.

42 H. Nagao, N. Komeda, M. Mukaida, M. Suzuki, K. Tanaka and others, *Inorg. Chem.*, 1996, **35**, 6809–6815.

43 G. Cavigliasso, R. Stranger, L. F. McClintock, S. E. Cheyne, P. M. Jaffray, K. E. Baxter and A. G. Blackman, *Dalton Trans.*, 2008, 2433–41.

44 A. G. Blackman, *Eur. J. Inorg. Chem.*, 2008, 2633–2647.

45 A. Beni, A. Dei, S. Laschi, M. Rizzitano and L. Sorace, *Chem. - A Eur. J.*, 2008, **14**, 1804–13.

46 K. G. Alley, G. Poneti, P. S. D. Robinson, A. Nafady, B. Moubaraki, J. B. Aitken, S. C. Drew, C. Ritchie, B. F. Abrahams, R. K. Hocking, K. S. Murray, A. M. Bond, H. H. Harris, L. Sorace and C. Boskovic, *J. Am. Chem. Soc.*, 2013, **135**, 8304–8323.

47 G. K. Gransbury, B. N. Livesay, J. T. Janetzki, M. A. Hay, R. W. Gable, M. P. Shores, A. Starikova and C. Boskovic, *J. Am. Chem. Soc.*, 2020, **142**, 10692–10704.

48 G. K. Gransbury, M. E. Boulon, S. Petrie, R. W. Gable, R. J. Mulder, L. Sorace, R. Stranger and C. Boskovic, *Inorg. Chem.*, 2019, **58**, 4230–4243.

49 Y. Zang, J. Kim, Y. Dong, E. C. Wilkinson, E. H. Appelman and L. Que, *J. Am. Chem. Soc.*, 1997, **119**, 4197–4205.

50 G. K. Gransbury and C. Boskovic, *Encycl. Inorg. Bioinorg. Chem.*, 2021.

51 T. Tezgerevska, K. G. Alley and C. Boskovic, *Coord. Chem. Rev.*, 2014, **268**, 23–40.

52 M. Meyer, *Acta Crystallogr. Sect. A*, 2012, **68**, S83.

53 M. Meyer, *Acta Crystallogr. Sect. A*, 2015, **71**, S496.

54 N. P. Cowieson, D. Aragao, M. Clift, D. J. Ericsson, C. Gee, S. J. Harrop, N. Mudie, S. Panjikar, J. R. Price, A. Riboldi-Tunnicliffe, R. Williamson and T. Caradoc-Davies, *J. Synchrotron Radiat.*, 2015, **22**, 187–190.

55 D. Aragão, J. Aishima, H. Cherukuvada, R. Clarken, M. Clift, N. P. Cowieson, D. J. Ericsson, C. L. Gee, S. Macedo, N. Mudie, S. Panjikar, J. R. Price, A. Riboldi-Tunnicliffe, R. Rostan, R. Williamson and T. T. Caradoc-Davies, *J. Synchrotron Radiat.*, 2018, **25**, 885–891.

56 L. Gaming and G. M. Sheldrick, *Acta Crystallogr. Sect. A*, 1999, **55**, 206.

57 G. M. Sheldrick, *Acta Crystallogr. Sect. A*, 2015, **71**, 3–8.

58 O. V. Dolomanov, L. J. Bourhis, R. J. Gildea, J. A. K. Howard and H. Puschmann, *J. Appl. Crystallogr.*, 2009, **42**, 339–341.

59 H. Puschmann, L. Bourhis, O. Dolomanov, R. Gildea and J. Howard, *Acta Crystallogr. Sect. A*, 2011, **67**, C593.

60 H. Puschmann and O. V. Dolomanov, *Acta Crystallogr. Sect. A*, 2019, **75**, E766.

61 L. A. Basal and M. J. Allen, *Front. Chem.*, 2018, **6**, 1–12.

62 M. Pinsky and D. Avnir, *Inorg. Chem.*, 1998, **37**, 5575–5582.

63 D. Casanova, J. Cirera, M. Llunell, P. Alemany, D. Avnir and S. Alvarez, *J. Am. Chem. Soc.*, 2004, **126**, 1755–1763.

64 D. I. Alexandropoulos, K. A. Schulte, K. R. Vignesh and K. R. Dunbar, *Chem. Commun.*, 2018, **54**, 10136–10139.

65 S. Goswami, S. Biswas, K. Tomar and S. Konar, *Eur. J. Inorg. Chem.*, 2016, **2016**, 2774–2782.

66 T. C. Jenks, M. D. Bailey, J. L. Hovey, S. Fernando, G. Basnayake, M. E. Cross, W. Li and

M. J. Allen, *Chem. Sci.*, 2018, **9**, 1273–1278.

67 B. A. Corbin, J. L. Hovey, B. Thapa, H. B. Schlegel and M. J. Allen, *J. Organomet. Chem.*, 2018, **857**, 88–93.

68 C. A. P. Goodwin, N. F. Chilton, L. S. Natrajan, M. E. Boulon, J. W. Ziller, W. J. Evans and D. P. Mills, *Inorg. Chem.*, 2017, **56**, 5959–5970.

69 P. K. Pal, S. Chowdhury, M. G. B. Drew and D. Datta, *New J. Chem.*, 2002, **26**, 367–371.

TOC

A structural, photophysical and electrochemical investigation of homoleptic $[Ln^{II}(Me_ntpa)_2]^{2+}$ complexes (Ln = Eu, Yb; n = 0, 2 and 3) reveals that the differing steric requirements of the Me_ntpa ligands modulate the ligand field experienced by the Ln^{II} metal ions and the resulting electronic properties of the complexes.